Exploring Visualization Methods for Complex Variables

Andrew J. Hanson[1] and Ji-Ping Sha[1]

1 **Computer Science Department and Mathematics Department**
Indiana University
Bloomington, IN 47405 USA
{hansona,jsha}@indiana.edu

Abstract

Applications of complex variables and related manifolds appear throughout mathematics and science. Here we review a family of basic methods for applying visualization concepts to the study of complex variables and the properties of specific complex manifolds. We begin with an outline of the methods we can employ to directly visualize poles and branch cuts as complex functions of one complex variable. $\mathbb{C}\mathbf{P}^2$ polynomial methods and their higher analogs can then be exploited to produce visualizations of Calabi-Yau spaces such as those modeling the hypothesized hidden dimensions of string theory. Finally, we show how the study of N-boson scattering in dual model/string theory leads to novel cross-ratio-space methods for the treatment of analysis in two or more complex variables.

1998 ACM Subject Classification I.3.5 Computational Geometry and Object Modeling, J.2 Physical Sciences and Engineering

Keywords and phrases Visualization, Complex Manifolds, High Dimensions

Digital Object Identifier 10.4230/DFU.SciViz.2010.90

1 Introduction

Mathematical visualization of issues involving complex variables is a fundamental problem that, sooner or later, is related to almost any problem in science. Our goal here is to review some general methods that can be used to make the abstract features of complex variables more concrete by exploiting computer graphics technology, and to illustrate these methods with some interesting applications. We begin with a number of general concepts, and conclude with some examples related to problems of mathematical physics motivated by string theory.

The basic methods for the representation of the shapes of homogeneous polynomial equations in $\mathbb{C}\mathbf{P}^2$ were explored in detail in ([3]), and this will be the starting point for many of our basic visualizations. We will also briefly summarize some more recent results of ([4]) treating some geometric objects arising naturally in the complex analysis of integrals appearing in the N-boson scattering amplitudes of the dual models of early string theory.

2 Visualizing Complex Analysis

Complex Numbers

We may think of a complex number in several ways. The most traditional form comes from the observation that, while the trivial equation $x^2 = 1$ can be solved in the domain of real numbers, the closely related equation $x^2 = -1$ cannot: one must introduce an "imaginary

Scientific Visualization: Advanced Concepts.
Editor: Hans Hagen; pp. 90–109

Dagstuhl Publishing
Schloss Dagstuhl – Leibniz Center for Informatics (Germany)

number" obeying $i^2 = -1$ in order to be able to represent the solutions to all algebraic equations of a single variable.

The most general form of the solution to an algebraic equation in one variable thus has two parts, a real part and an imaginary part, which can be written in terms of two real numbers x and y as

$$z = x + iy \ . \tag{1}$$

We also introduce the complex conjugation operation,

$$\overline{z} = x - iy \ , \tag{2}$$

which in turn leads to the concept of the modulus-squared,

$$z\overline{z} \equiv |z|^2 = x^2 + y^2 \ . \tag{3}$$

The essential properties of products of complex numbers follow directly from the properties of the symbol i, yielding

$$z_1 z_2 = (x_1 + iy_1)\,(x_2 + iy_2) = (x_1 x_2 - y_1 y_2) + i\,(x_1 y_2 + x_2 y_1) \ . \tag{4}$$

A more formal way of writing this would be to consider Eq. (4) as a realization of an abstract algebra relating pairs of numbers, where the corresponding (commutative, associative) algebra is defined as

$$(x_1,\, y_1) \star (x_2,\, y_2) = (x_1 x_2 - y_1 y_2,\, x_1 y_2 + x_2 y_1) \ . \tag{5}$$

Equations (4) and (5) are indistinguishable in any mathematical sense, though some practitioners may feel strongly about being more comfortable with one or the other.

For completeness, we note that another unique property of complex numbers is that, besides the trivial case of real multiplication, only complex multiplication is both commutative and preserves the value of the modulus under multiplication,

$$|z_1 z_2| = |z_1|\,|z_2| \ . \tag{6}$$

2.0.0.1 Visualizing a Complex Point

Once we have Eq. (1), we may ask immediately how we visualize a complex point. One approach is that of Figure 1(a), which simply treats x and y as Cartesian variables, and so every complex number is depicted as a point in the 2D plane. However, this does not allow us to easily treat infinity, which is a critical element in the mathematical analysis of functions of a complex variable. Thus Figure 1(a) is only a local view of the actual manifold that mathematicians refer to as "the complex line" because of its one-dimensional complex nature, and that physicists and engineers, for example, would refer to as the "complex plane" because of its two-dimensional real nature. In order to treat the space of one complex variable in a way that infinity is no longer a special point, and can be included naturally in all the tasks of complex analysis, we must find a way to express coordinates on the space in a way that is more general than simple Cartesian coordinates. The solution to this problem is to treat the representation of one complex variable using *one-dimensional complex projective space* or $\mathbb{C}\mathbf{P}^1$, which is the space of *pairs* of complex numbers $(z_0,\, z_1)$ that are taken to be equivalent under multiplication by any nonvanishing complex number λ, which is to say

$$(z_0,\, z_1) \sim (\lambda z_0,\, \lambda z_1) \ . \tag{7}$$

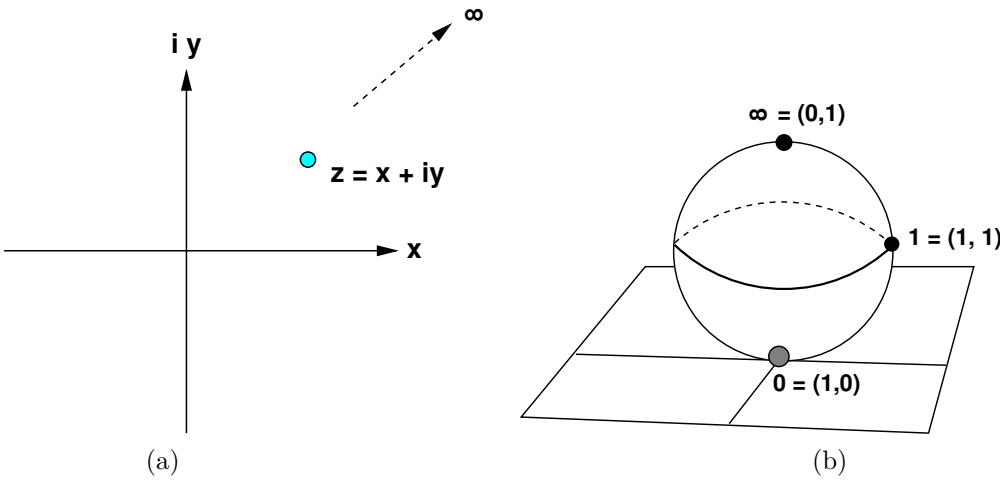

Figure 1 (a) The complex plane. (b) The full space of one complex variable, the one-dimensional complex projective space $\mathbb{C}\mathbf{P}^1$, which is topologically the same as an ordinary sphere, and is thus also known as the Riemann sphere.

Note that this is a two-ended ray of equivalences, since λ may take either sign. We see that in Figure 1(a) we have chosen, e.g., the local coordinates $z_0 = 1$ and $z = z_1/z_0 = z_1$. The point at ∞ now has a precise realization as the coordinate that results when we let $z_0 \to 0$; however, in the context of complex projective space, we never allow this to happen, since we can always write "infinity" as the finite homogenous pair $(0, z_1)$. There are thus essentially two patches in the coordinate system, one where z_0 is allowed to be zero, but not z_1, so the coordinate system is $(z, 1)$, and a second where z_1 is allowed to be zero, but not z_0, so the coordinate system is $(1, z)$. The origin of each of these coordinate systems is the infinity of the other, and the two coordinate systems at all other points are related by multiplication by z_1/z_0 or by z_0/z_1.

When we make *local pictures*, therefore, we must choose one of these two coordinate systems, and accept that we cannot draw at infinity until we change coordinate systems. The entire complex plane thus consists of two parts:

- **North pole.** ($z_1 = 0 \to$ OK, but $z_0 \neq 0$).
- **South Pole.** ($z_0 = 0 \to$ OK, but $z_1 \neq 0$).

When we patch these two neighborhoods together around the equator, we find that the result is a topological sphere, so $\mathbb{C}\mathbf{P}^1 \sim \mathbf{S}^2$, as shown schematically in Figure 1(b).

2.0.0.2 Fixing the coordinate system

Complex projective space admits a standard group of transformations, $\mathbf{PGL}(2, \mathbb{C})$ or the linear-fractional transformations, that parameterize all possible transformations of the coordinate system on $\mathbb{C}\mathbf{P}^1$. The specific transformation on the homogeneous coordinates can be written using the $\mathbf{PGL}(2, \mathbb{C})$ matrix elements

$$[M] = \begin{bmatrix} \alpha & \beta \\ \gamma & \delta \end{bmatrix} , \tag{8}$$

with $\det M \neq 0$, as

$$\begin{bmatrix} z_0' \\ z_1' \end{bmatrix} = M \cdot \begin{bmatrix} z_0 \\ z_1 \end{bmatrix}$$

or

$$(z_0',\, z_1') = (\alpha z_0 + \beta z_1,\, \gamma z_0 + \delta z_1) \ , \tag{9}$$

in the homogeneous, ray-equivalent coordinates, or as

$$z' = \frac{\alpha z_0 + \beta z_1}{\gamma z_0 + \delta z_1} \tag{10}$$

in the $\gamma z_0 + \delta z_1 \neq 0$ set of inhomogeneous coordinates.

The group of linear fractional transformations thus has three free complex parameters that can be used to map any three complex points in the complex plane to any chosen points to fix the degrees of freedom under the map. As illustrated in Figure 1(b), these are conventionally chosen in the following way:

- "0" is projective $(1, 0)$,
- "1" is projective $(1, 1)$, and
- "∞" is projective $(0, 1)$.

2.1 Cross Ratios and Cross-Ratio Coordinates

An important feature of complex projective space is that there is a family of *invariants* under the linear fractional transformations (9) known as the *cross ratios*, defined as follows:

$$u(w, x, y, z) = \frac{(w-y)}{(w-z)} \Bigg/ \frac{(x-y)}{(x-z)} = \frac{(w-y)(x-z)}{(w-z)(x-y)} \ . \tag{11}$$

In particular, one can verify that there are two distinct cross ratios of four variables,

$$u_1 \quad = \quad u(z, z_1, z_0, z_2) = \frac{(z-z_0)(z_1-z_2)}{(z-z_2)(z_1-z_0)} \tag{12}$$

$$u_2 \quad = \quad u(z_1, z_2, z, z_0) = \frac{(z_1-z)(z_2-z_0)}{(z_1-z_0)(z_2-z)} \tag{13}$$

that are related by the constraint

$$1 = u_1 + u_2 \ . \tag{14}$$

Since there are three remaining complex degrees of freedom in the $\mathbf{PGL}(2, \mathbb{C})$ matrix $[M]$ after accounting for projective equivalence, we can exhaust those degrees of freedom by *choosing a coordinate system* on $\mathbb{C}\mathbf{P}^1$ that fixes three complex points. This fact ties in with the definition of the group-invariant cross ratios because it allows us to fix three of the variables in the cross ratio to be, for example, 0, 1, and ∞, thus fixing

$$u_1 \quad = \quad u(z, 1, 0, \infty) = z \tag{15}$$

$$u_2 \quad = \quad u(1, \infty, z, 0) = 1 - z \ . \tag{16}$$

2.1.0.3 Cross-ratio space

However, even this is not the whole story. As pointed out in ([4]), from Eq. (14) we can deduce the existence of yet another projective space, the *cross-ratio space*, which results from creating a new set of homogeneous coordinates, this time in $\mathbb{C}\mathbf{P}^2$, by realizing that we must add a third variable, u_0, to Eq. (14) to make it homogenous:

$$u_0 = u_1 + u_2 \ . \tag{17}$$

This equation can be solved projectively in three different sets of variables, corresponding to choosing the local coordinates $u_0 = 1$, $u_1 = 1$, or $u_2 = 1$, and three intervals in inhomogeneous coordinates as $A = [0, 1]$, $B = [1, \infty]$, and $C = [-\infty, 0]$. The triples of variables solving the constraint equation (17) can then be written

$$\begin{aligned} A(t): &\quad [1,\, t,\, (1-t)] \\ B(t): &\quad [(1-t),\, 1,\, -t] \\ C(t): &\quad [-t,\, (1-t),\, -1]\ . \end{aligned} \tag{18}$$

The variables of region A solve $1 = u_1 + u_2$ with $u_1 = t$, B solves $1 = u_1 + u_2$ with $u_1 = 1/(1-t)$ when all is multiplied by $(1-t)$, and C solves $1 = u_1 + u_2$ with $u_1 = (t-1)/t$ when all is multiplied by t. We note that $C(1) = -A(0)$, so that in fact we have a double covering of the constraint space: the constraint equation solutions must be adjoined to their negatives to form a piecewise continuous curve in $\mathbb{C}\mathbf{P}^2$.

This concludes our introduction to the basic concepts we need to build various visualizations related to a single complex variable. Next we work out some examples in complex analysis.

2.2 Visualizing a Simple Pole

The simplest example of a complex function is a constant function,

$$z = a + ib.$$

Choosing a particular local $\mathbb{C}\mathbf{P}^1$ coordinate system allows us to plot this as a point in a plane as in Figure 1(a). However, even this is not quite as simple as it looks. First we recall that ordinary real graphs of functions are written as

$$y = f(x)\ ,$$

so that we use one space dimension to graph the value of the independent variable and a second one to graph the result. Thus the correct complex analog would involve *two* complex variables: z describing the value of the independent variable, and, say,

$$w = f(z) = \mathrm{Re}\, f(z) + i\, \mathrm{Im}\, f(z)$$

to describe the (complex) result of evaluating the function. Thus, we might consider the graphing process to be described more clearly using two variables, $z_1 = x_1 + iy_1$ and $z_2 = x_2 + iy_2$, where

$$z_2 = f(z_1)\ . \tag{19}$$

We can easily see how this works with the classic example of a simple pole at the origin,

$$\frac{1}{z} = \frac{x - iy}{x^2 + y^2}\ .$$

Using the two-variable form, we find that the result involves four variables, (x_1, y_1, x_2, y_2), and one complex or two real equations, so the shape described is a surface with components given by the real and imaginary parts of the following:

$$z_2 = x_2 + iy_2 = \frac{1}{z_1} = \frac{x_1 - iy_1}{x_1^2 + y_1^2}\ . \tag{20}$$

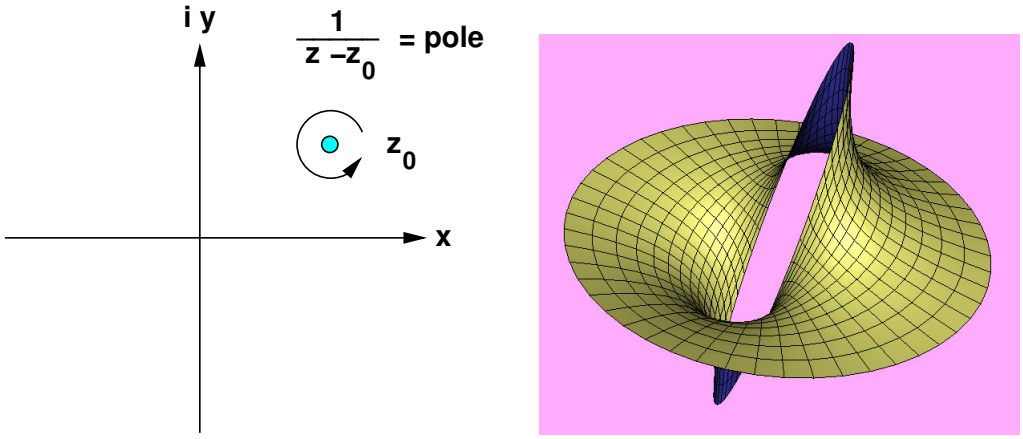

(a) (b)

Figure 2 (a) Conventional picture of a complex pole $f(z) = 1/(z - z_0)$ at z_0, indicating the positive sense of a contour to pick up the residue. (b) Visualizing the geometric shape of a complex pole $w = 1/z$ showing $\mathrm{Re}\, w$ as a function of z. The imaginary part looks basically the same.

The result must be projected from 4D to 3D to be rendered using standard graphics methods. In Figure 2, we show the location of a general pole $f(z) = 1/(z - z_0)$ using a textbook 2D complex analysis plot, and then show the visualization of the complex surface corresponding to the pole using $\mathrm{Re}\, z_2 = x_2$ as the third axis.

Remark: The analysis of a pole typically involves one more step, namely the description of a circular contour integral surrounding the pole. From the classic theorems of complex analysis, this integral

$$\int_{\text{closed circle}} \frac{dz}{z}$$

vanishes if the contour does not enclose the pole, and has the constant value $2\pi i$ as long as the contour encloses the pole. The proof is trivial in polar coordinates with $z = r\exp(i\theta)$:

$$\int_{\text{circle with radius } r} \frac{dz}{z} = \int_0^{2\pi} \frac{ire^{i\theta}d\theta}{re^{i\theta}} = 2\pi i \ .$$

2.3 Integrating with Branch Cuts

Moving on from simple poles, we next examine functions with multiple roots, and hence multiple branches of the Riemann surfaces that are needed to precisely define the functions. The square root already has ample complexity to challenge our visualization technology. If we consider the contour integral of the function $w = \sqrt{1 - z^2}$ along a path that passes around $z = +1$, we find the standard textbook drawing in Figure 3 describing the integral

$$\int_{a+b} dz\, \sqrt{1 - z^2} \ .$$

The main characteristic distinguishing a branch cut in analysis is that, while, e.g., the phase of the function changes by a full (2π) along a path going around a pole, it changes by a precise fraction, namely $2\pi/n$, along a path going from one side of an n-th root branch point to the other. Thus, for example, the relative phase between the integrand on the path of the

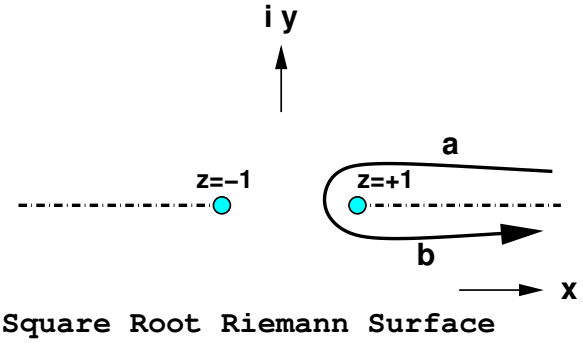

Figure 3 Complex contour integral around the square-root branch point of $\sqrt{1-z^2}$ at $z=+1$.

a branch and the path of the b branch for the square root branch cut shown in Figure 3 is

$$e^{2\pi i/2} = -1 \ .$$

Here, once again, we need to go beyond conventional diagrams such as Figure 3 to create a useful visualization. One approach to functions with multiple branch points is to realize that the Riemann surface to be displayed should not just represent a single branch, e.g.,

$$w = +\sqrt{1-z^2} \tag{21}$$

or

$$w = -\sqrt{1-z^2} \ , \tag{22}$$

but should represent *all* branches. With a little thought we can see that everything is summarized nicely in the equation

$$w^2 + z^2 = 1 \ . \tag{23}$$

There are many different ways to plot this surface (remember, 4 real variables, with 2 real equations means it is a surface), including just using the separate pieces from Eqs. (21) and (22) directly. We typically prefer the methods introduced in ([3]), which will be described shortly, and which recreate the entire surface from a very simple fundamental domain via complex phase transformations around the fixed points of the surface. The basic problem goes back once again to the difference between homogeneous and inhomogeneous coordinates: we should really be looking at Eq. (23) as a homogeneous equation in $\mathbb{C}\mathbf{P}^2$ of the form

$${z_0}^2 + {z_1}^2 + {z_2}^2 = 0 \ . \tag{24}$$

Choosing any one of the $\mathbb{C}\mathbf{P}^2$ variables (z_0, z_1, z_2) to be a constant ($z_0 = i$ is just as good as $z_0 = 1$) gives a partial shape that does not include infinity (where the constant variable vanishes, e.g., $z_0 \to 0$). Thus we are left with holes in the surface that are represented as rings that go off to infinity when we plot the surface using a local pair of inhomogeneous variables as in Figure 4. The square root branch points and cuts can be explicitly seen in the projection of Figure 4 as the ending points of the X-shaped crossings.

2.4 Visualizations of Homogeneous Polynomials in $\mathbb{C}\mathbf{P}^2$

The square root Riemann surface is a special case of a general family of polynomials that are of interest. Here we review the properties and visualization methods for the simplest

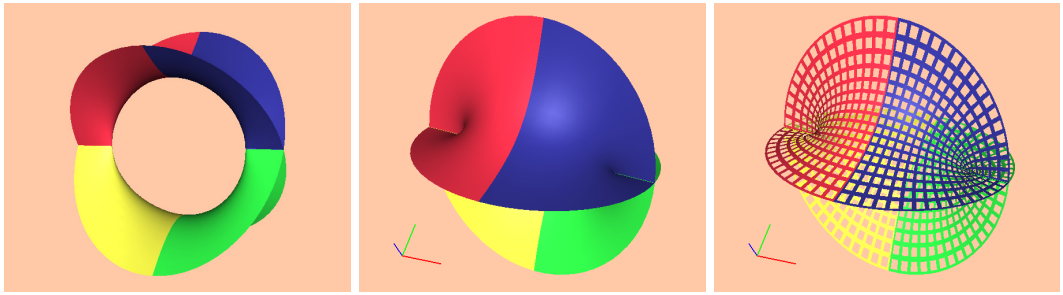

Figure 4 Assorted views of the full square-root Riemann surface with Re w projected to the 3rd axis. The surface is a topological sphere, but the local inhomogeneous coordinates obscure that fact since there are two rings going off to the surface at infinity. The inner ends of the X-shaped crossings are the branch points.

homogeneous polynomials that arise in the study of $\mathbb{C}\mathbf{P}^2$. Starting from the n-th root of a polynomial of one complex variable with zeros at the n roots of unity, that is

$$w = (1 - z^n)^{1/n} \tag{25}$$

and following the same procedure as for the square root, we arrive at the corresponding homogeneous polynomial in $\mathbb{C}\mathbf{P}^2$:

$$z_0{}^n + z_1{}^n + z_2{}^n = 0 \ . \tag{26}$$

As we have noted, there are a variety ways to solve this equation, including:

- n **roots:** Set $z_0{}^n = -1$ and solve for the n roots of $(1 - z^n)^{1/n}$ (which are found by multiplying by a phase $\exp(2\pi ik/n)$, $k = 0, \ldots, n-1$).
- **Spinor variables:** Parameterize the solution using the variables typically used to define null spinors, $w_0{}^2 + w_1{}^2 + w_2{}^2 = 0$ ([1]):
  $$\begin{aligned} z_0 &= \left(i(x^2+y^2)\right)^{2/n} \\ z_1 &= \left(x^2-y^2\right)^{2/n} \\ z_2 &= (2xy)^{2/n} \ . \end{aligned}$$
  Because of the projective equivalence, only n^2 of the n^3 phase choices available here are meaningful.
- n^2 **roots:** In the method of ([3]), the relative phases of n^2 different congruent patches tie together to create the full topological surface, where the obvious locations of the fixed points of the z_1 and z_2 phase transformations expose many key features of the surface. The method starts as before by setting $z_0{}^n = -1$. Then we exploit the complex trigonometric identity

  $$\cos(\theta + i\xi)^2 + \sin(\theta + i\xi)^2 = 1$$

  to define one patch, the fundamental domain, as the quadrant where θ gives a positive real part for cos and sin, namely $0 \le \theta \le \pi/2$ and $-\xi_{\max} \le \xi \le +\xi_{\max}$. Thus the first and most elementary of the n^2 patches is
  $$\begin{aligned} w_1 &= (\cos(\theta + i\xi))^{2/n} \\ w_2 &= (\sin(\theta + i\xi))^{2/n} \ . \end{aligned}$$
  The remaining patches are found by making phase transformations on both z_1 and z_2 until the entire surface is covered; all the patches are then labeled by the n^2 integer pairs

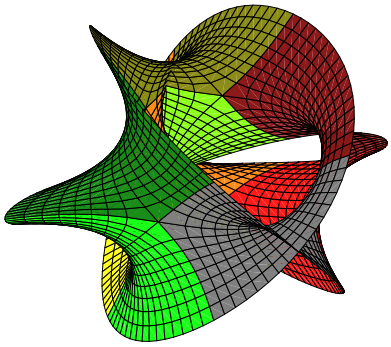

Figure 5 $n = 3$ in $\mathbb{C}\mathbf{P}^2$: The cubic is a torus.

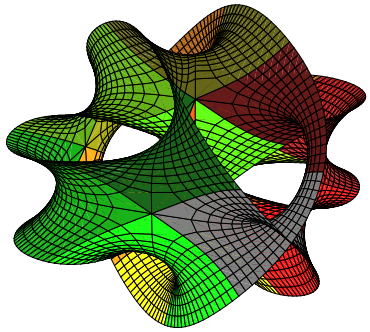

Figure 6 $n = 4$ in $\mathbb{C}\mathbf{P}^2$: The quartic is a section of the **K3** surface, a 4-manifold.

(k_1, k_2), where $k_1 = 0, \ldots, n-1$, $k_2 = 0, \ldots, n-1$, and the parametric solutions of the equations become

$$\begin{aligned} z_1 &= \exp(2\pi i k_1/n) w_1 \\ z_2 &= \exp(2\pi i k_2/n) w_2 \ . \end{aligned}$$

Typical results are shown in the Figures as follows:

- **Cubic Torus.** The cubic is topologically a torus (genus 1), though it is hard to see due to the infinities in local coordinates. It is also technically the standard polynomial in $\mathbb{C}\mathbf{P}^2$ that is a Calabi-Yau space. See Figure 5.
- **Slice of K3 Quartic.** K3 is described by the quartic polynomial of complex dimension 2 (4 real dimensions) in $\mathbb{C}\mathbf{P}^3$. This is the *unique simply-connected* Calabi-Yau 4-manifold, and we can write the equation locally as

$$(z_1)^4 + (z_2)^4 + (z_3)^4 = 1 \ . \tag{27}$$

This is one complex constraint in 3D complex space, and thus is a manifold with 2 complex, 4 real, dimensions. Setting, e.g., $z_3 = 0$, gives a slice that is a surface in $\mathbb{C}\mathbf{P}^2$ with genus 3. See Figure 6.

- **Slice of Calabi-Yau Quintic.** It is hypothesized that 10-dimensional string theory includes 4 dimensions of space-time and 6 dimensions that are curled up into a Calabi-Yau space at the scale of the Planck length. A popular (but by no means unique) candidate for this space is the quintic in $\mathbb{C}\mathbf{P}^4$ given locally by the equation

$$(z_1)^5 + (z_2)^5 + (z_3)^5 + (z_4)^5 = 1 \ . \tag{28}$$

This is one complex constraint in 4D complex space, and thus is a manifold with 3 complex, 6 real, dimensions. Setting, e.g., $z_3 = z_4 = 0$, gives a slice that is a surface in $\mathbb{C}\mathbf{P}^2$ with genus 6. See Figure 7.

In general, it can be shown that every homogeneous polynomial of degree $N+1$ in $\mathbb{C}\mathbf{P}^N$ is in fact a Calabi-Yau space and therefore admits a Ricci-Flat metric. Calabi conjectured and Yau proved the existence of these metrics ([8]), but, except for trivial cases such as the $\mathbb{C}\mathbf{P}^2$ cubic torus, none are explicitly known. In Table 1, we summarize this family of spaces.

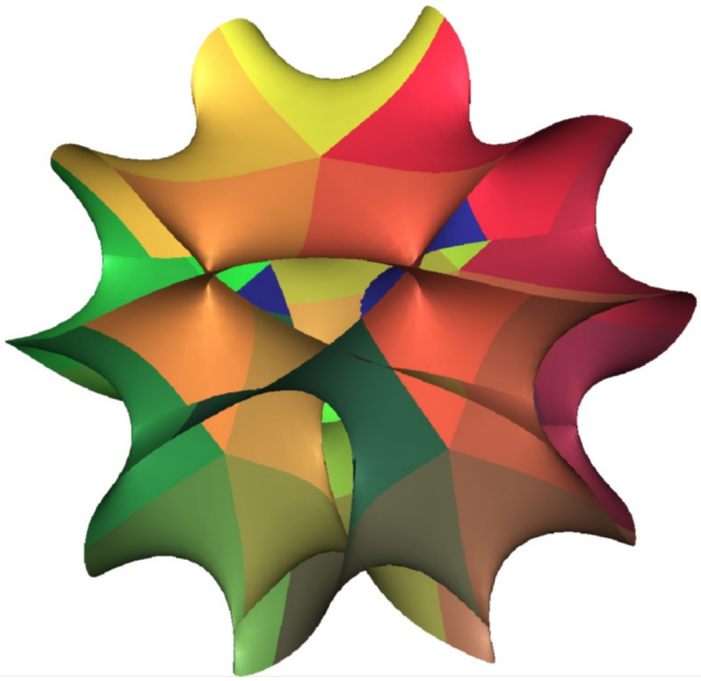

Figure 7 $n = 5$ in $\mathbb{C}\mathbf{P}^2$: The quintic is a section of the Calabi-Yau quintic, the 6-manifold proposed for the hidden dimensions of string theory.

Table 1 Road map of the simple homogeneous polynomial Calabi-Yau spaces.

N	CP	deg(f)	$\mathbb{C}$ dim	$\mathbb{R}$ dim	*Remarks*
1	$\mathbb{C}\mathbf{P}^1$	2	0	0	$z = \pm 1$, the 0-sphere $\mathbf{S}^0$
2	$\mathbb{C}\mathbf{P}^2$	3	1	2	flat torus $\mathbf{T}^2$
3	$\mathbb{C}\mathbf{P}^3$	4	2	4	K3 surface
4	$\mathbb{C}\mathbf{P}^4$	5	3	6	CY String Theory quintic
N	$\mathbb{C}\mathbf{P}^N$	N+1	N-1	2(N-1)	Solution of $\sum_{i=1}^{N} (z_i)^{N+1} = 1$

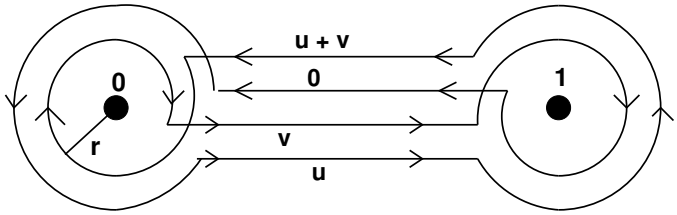

Figure 8 The Euler Beta Function has this remarkable *unshrinkable* contour representation due to Pochhammer.

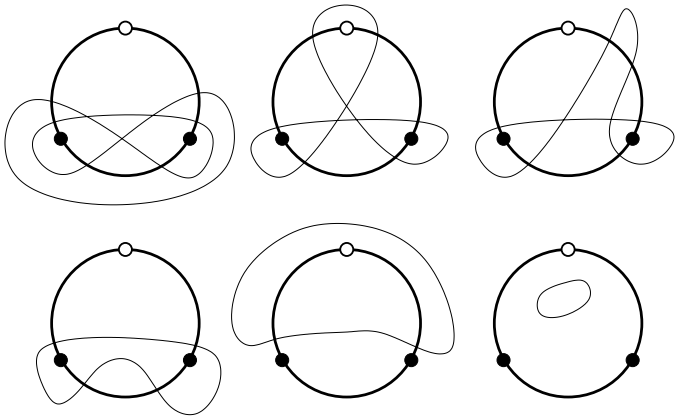

Figure 9 When $u + v = 0, -1, \ldots$, deformation through ∞ has no obstruction: one can simply unloop the contour and pass through the $[0, 1]$ branch line, resulting in a contour that *shrinks to zero.*

2.5 Visualizing Infinite Riemann Surfaces: the Pochhammer Contour

The next challenge is to consider the problems of visualizing complex functions that, unlike the square root and its analogs, may have infinite Riemann surfaces. There is a classic example from the 19th century that provides all the features relevant to this problem. The Euler Beta Function can be represented as the improper integral

$$B(u, v) = \int_0^1 x^{u-1}(1-x)^{v-1}\, dx \tag{29}$$

with the analytic continuation

$$B(u, v) = \frac{\Gamma(u)\Gamma(v)}{\Gamma(u+v)}\ . \tag{30}$$

Now, if one considers the integrand of Eq. (29) as a branched complex function $z^{u-1}(1-z)^{v-1}$ defining a Riemann surface, one finds branch points at $z = 0$ and at $z = 1$ with possibly infinite branchings if u or v should be irrational. However, in 1890 Pochhammer was clever enough to see this not as a problem but as an opportunity to define a new kind of contour integral that was not sensitive to infinite branchings ([5]). In Figure 8 we show the usual planar sketch of Pochhammer's Contour, from which a little analysis allows us to compute its value as

$$\epsilon(u, v) = (1 - e^{2\pi i u})(1 - e^{2\pi i v}) \int_0^1 x^{u-1}(1-x)^{v-1}\, dx \tag{31}$$

$$= (1 - e^{2\pi i u})(1 - e^{2\pi i v}) B(u, v)\ . \tag{32}$$

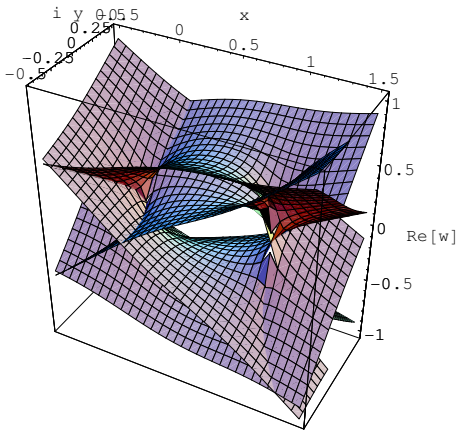

Figure 10 Sample Riemann surface for the B_4 integrand – multiple branch coverings spiral to infinity.

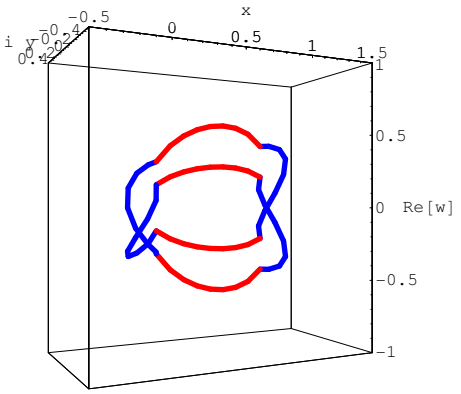

Figure 11 The corresponding embedded Pochhammer contour is a *commutator*, encircling each branch point *twice*.

Through an interesting trick of complex analysis, one can determine the zeroes of the function directly to occur when $u+v=0,-1,\ldots$: at these values, the contour can be "pulled over" the point at infinity as shown in Figure 9 and deformed to an equivalent vanishing loop. These zeroes can be confirmed explicitly from the analytic continuation Eq. (30).

Finally, we can explicitly create a function representing the Riemann surface of the Euler Beta function integrand.

$$\beta(z;\,u,v)=z^{u-1}(1-z)^{v-1} \tag{33}$$

and create a 3D projection with, e.g., the vertical axis given by $\mathrm{Re}\,\beta(z;\,u,v)$. Figures 10 and 11 show a section of a branched covering that could in principle spiral indefinitely, along with the closed Pochhammer loop that can be traced on the Riemann surface, no matter how complex. Figure 12 superimposes these on the same space to illustrate the context.

3 Extending $\mathbb{C}\mathrm{P}^2$ Visualization Methods to $\mathbb{C}\mathrm{P}^3$

Our next objective is to see how we can create some basic images of the K3 surface that give more global information than the 2D slice representation that we saw in Figure 6. We recall that K3 can be represented in general as a homogeneous quartic polynomial in $\mathbb{C}\mathbf{P}^3$ in the form

$$z_0{}^4+z_1{}^4+z_2{}^4++z_3{}^4=0\ , \tag{34}$$

which reduces after division by $z_0\neq 0$ (or equivalently, after division by z_1, z_2, or z_3) to Eq. (27). Even though this is a 4-manifold (after division, 6 real variables and two real constraint equations), we can pick out some of its global, non-slicing, properties by considering what amounts to the "real subspace" of the parameterization.

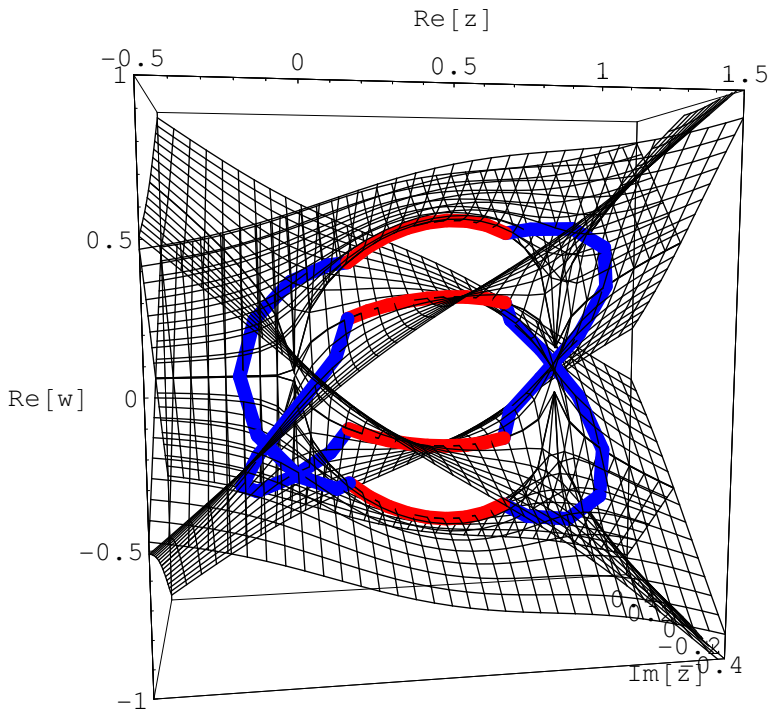

Figure 12 Pochhammer contour plotted directly on the Riemann surface.

3.1 $\mathbb{C}\mathbf{P}^2$ Example

We can see an example of a dimensional reduction in the $\mathbb{C}\mathbf{P}^2$ case by remembering that in the n^2 patch method ([3]), each patch is parameterized as

$$\begin{aligned} z_1 &= (\cos(\theta + i\xi))^{2/n} \\ z_2 &= (\sin(\theta + i\xi))^{2/n} \end{aligned}$$

with $0 \leq \theta \leq \pi/2$, so, with the imaginary part of the argument approaching zero ($\xi \approx 0$), the complex variables (z_1, z_2) become purely real and describe a circular quarter arc from $z_1(\theta = \pi/2) = 0$ to $z_2(\theta = 0) = 0$. Since, at $z_1 = 0$, multiplying by the z_1 phase $\exp(2\pi i k_1/n)$ leaves zero as a fixed point, there will be n copies of the circular arc fanning out from $z_1 = 0$ to n copies of the intersection point $z_2 = 0$. (Note: these may be understood simply as the roots of $(z_1)^n + (z_2)^n = 1$ with either $z_1 = 0$ or $z_2 = 0$.)

In Figure 13, we show the $z_1 = 0$ intersection points as green cubes, the $z_2 = 0$ intersection points as red cubes, and let ξ have a finite range to show the surface shape near the core. In Figure 14, we set $\xi \approx 0$ to expose the n^2 "real core" curves forming the graph of the surface skeleton in this local inhomogeneous coordinate system. Note that this is not quite a topologically symmetric structure because infinity has been treated specially in this coordinate system, but a great deal of the structure, e.g., the degree of the polynomial, is clearly exposed.

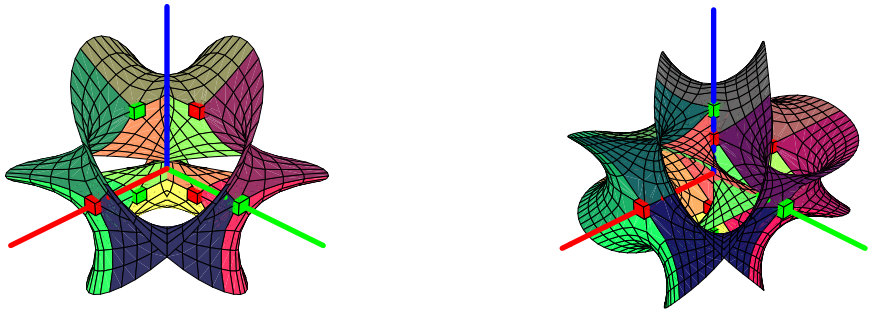

Figure 13 Left: $n = 3$ cubic. Right: $n = 4$ quartic. Red and Green points represented as small cubes indicate where the zeros of z_1 and z_2 pass through the surface; each of $z_2 = 0$ Red points is connected to all n copies of the $z_1 = 0$ Green points, and vice versa, through the "real" central line of each of the n^2 patches.

Figure 14 Shrinking the complex extent of the surface parameterization so that only the "real core" curves remain shows a connected graph of n^2 arcs connecting the $2n$ nodes.

3.2 The K3 "Real Core"

The representation of the K3 surface as a fourth-degree homogeneous polynomial in $\mathbb{C}\mathbf{P}^3$, like the general case of the $\mathbb{C}\mathbf{P}^2$ polynomials described earlier, can be solved in a variety of ways. Here we will focus on generalizing the n^2 patch method ([3]) to $\mathbb{C}\mathbf{P}^3$, which turns out to lead naturally to n^3 patches of dimension 4 (and for $\mathbb{C}\mathbf{P}^N$, to n^N patches of dimension $2(N-1)$). Thus the basic equation for which we seek a 4-parameter parametric form is

$$(z_1)^4 + (z_2)^4 + (z_3)^4 = 1 \ . \tag{35}$$

Following the complexified circle ($\mathbf{S}^1$) method used for $\mathbb{C}\mathbf{P}^2$, we arrive at a 4-manifold parameterization based on the complexified sphere $\mathbf{S}^2$, namely

$$(\cos\theta \sin\phi, \sin\theta \sin\phi, \cos\phi) \tag{36}$$

with $0 \le \phi \le \pi$, $0 \le \theta < 2\pi$. For the full 4D patch, we would complexify the angular variables as $\theta \to \theta + i\xi$, $\phi \to \phi + i\rho$ to get exponential growth towards infinity. To retain the "real skeleton" surface analogous to the network of edges shown in Figure 14 for $\mathbb{C}\mathbf{P}^2$ polynomials, all we need to do is recast the real equation (36) in the form

$$\begin{aligned} w_1 &= (\cos\theta \sin\phi)^{2/n} \\ w_2 &= (\sin\theta \sin\phi)^{2/n} \\ w_3 &= (\cos\phi)^{2/n} \ , \end{aligned}$$

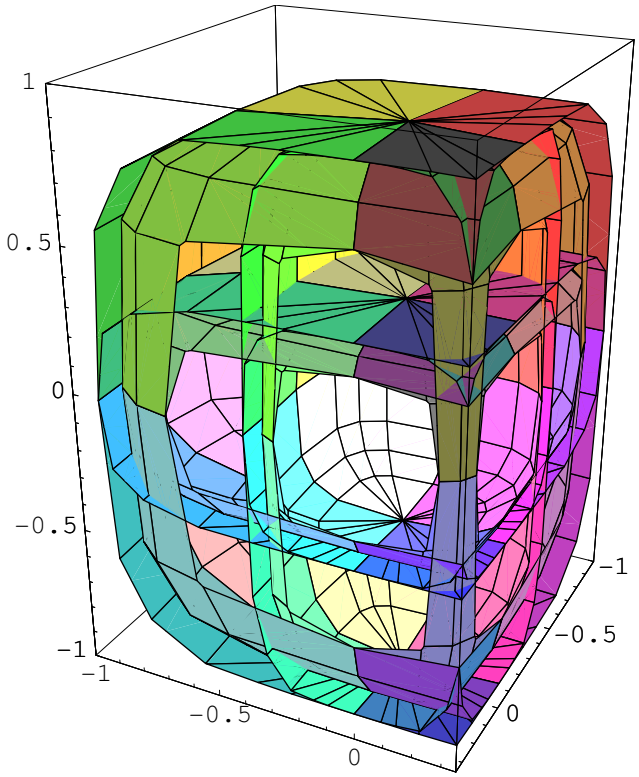

Figure 15 The "real core" of the quartic K3 Calabi-Yau space, delimited by $4^3 = 64$ spherical triangles. Each spherical triangle is bounded by the intersections of the zeros of the three local complex variables with the K3 surface (a 4-manifold).

with $n = 4$ selecting the K3 fundamental domain ($2/n = 2/4 = 1/2$ so each term is a square root). The remaining patches are found by making phase transformations on (z_1, z_2, z_3) until the entire surface is covered; all the patches are then labeled by the $n^3 = 64$ integers (k_1, k_2, k_3), where $k_i = 0, 1, 2, 3$ and the parametric solutions of the equations become

$$\begin{aligned} z_1 &= \exp(2\pi i k_1/4) w_1 \\ z_2 &= \exp(2\pi i k_2/4) w_2 \\ z_3 &= \exp(2\pi i k_3/4) w_3 \ . \end{aligned}$$

The result is a collection of octants of the sphere, spherical triangles that fan out four at a time from the curves where $z_1 = 0$, $z_2 = 0$, and $z_3 = 0$ intersect the manifold. The result is depicted in Figure 15, where part of the shape is cut away so that the interior "fanning out" is made visible. We remark that just as Figure 14 appears to have non-manifold triple or quadruple intersections, but in fact, when complexified, yields the smoothed continuous surface of Figure 13, we need to imagine that in 4D, Figure 15 also extends completely smoothly away from the 4-way fan-out junctions.

3.2.0.4 Regular global tessellations

The representations shown here are local and are limited in their effectiveness for exposing the overall topology of the polynomials in $\mathbb{C}\mathbf{P}^2$ and $\mathbb{C}\mathbf{P}^3$, etc. Extending these limited local representations to global tessellations with maximal symmetries is a subject of ongoing research.

4 Two Complex Variables and the Dodecahedron

Finally, we review our approach to creating visualizations for problems arising in many-complex-variable analysis, outlining the two-complex-variable case as our main example ([4]). We begin with the N-particle bosonic scattering amplitude of the original dual model, the precursor to string theory, which is given by the integral

$$B_N = \int \cdots \int_{\text{vol}} \left[\prod_{ij} u_{ij}^{\alpha_{ij}-1} \right] \frac{\prod_k du_{1k}}{(1-u_{14}) \cdots (1-u_{1,N-1})}$$

The N-point cross-ratios u_{ij} obey a set of constraints that is non-linear except for the 4-particle case B_4, which in fact is the Euler Beta function treated earlier:

$$u_{ij} = 1 - \prod_{m=i+1}^{j-1} \prod_{n=j+1}^{i-1} u_{mn} \ .$$

These constraints define manifolds in $\mathbb{C}\mathbf{P}^{N(N-3)/2}$ that provide new insight into the nature of the analytic continuation of these integrals.

The $N = 5$ case is the simplest non-trivial example that we can work out explicitly; the corresponding improper integral is two-dimensional,

$$\begin{aligned} B_5(\alpha_1, \alpha_2, \alpha_3, \alpha_4, \alpha_5) = & \\ = & \int_0^1 \int_0^1 s^{\alpha_1 - 1} t^{\alpha_2 - 1} (1-s)^{\alpha_3 - 1} (1-st)^{\alpha_4 - \alpha_3 - \alpha_5} (1-t)^{\alpha_5 - 1} \, ds \, dt \\ = & \iint (z_1)^{\alpha_1 - 1} (z_2)^{\alpha_2 - 1} (z_3)^{\alpha_3 - 1} (z_4)^{\alpha_4 - 1} (z_5)^{\alpha_5 - 1} \, ds \, dt / (1-st) \ , \end{aligned} \tag{37}$$

and thus must eventually be treated using two complex variables.

The B_5 cross-ratio constraints are quadratic,

$$\begin{aligned} 1 - z_1 - z_3 z_4 &= 0 \\ 1 - z_2 - z_4 z_5 &= 0 \\ 1 - z_3 - z_5 z_1 &= 0 \\ 1 - z_4 - z_1 z_2 &= 0 \\ 1 - z_5 - z_2 z_3 &= 0 \ , \end{aligned} \tag{38}$$

and, in these variables, there are twelve different possible integration domains of Eq. (37) that we can initially represent as in Figure 16. Using $\mathbb{C}\mathbf{P}^5$ cross-ratio variables, we would properly represent these equations as ${z_0}^2 - z_0 z_1 - z_3 z_4 = 0$, etc., but we will omit the details here.

Each individual region, when plotted using Eq. (38), is not simply a square or triangle as one might guess from the Cartesian variable plot in Figure 16, but is actually a pentagon, as shown in Figure 17

The resulting figure is a "blown-up" dodecahedral manifold formed from twelve pentagons, but this dodecahedron, shown in Figure 18, is quite different topologically from the familiar Platonic dodecahedron, and in fact has Euler characteristic $\chi = -3$, so it is a surface

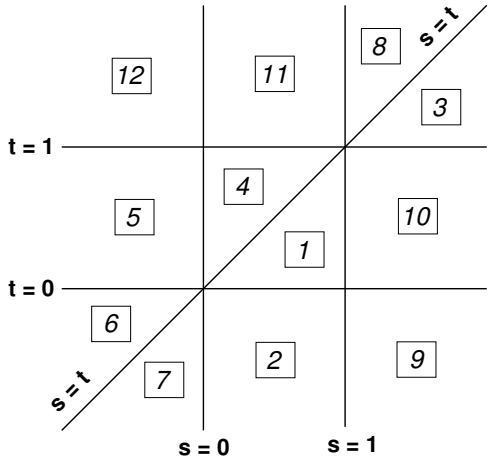

Figure 16 The 12 connected components of the domain of parameters for the set of 5-point cross-ratios.

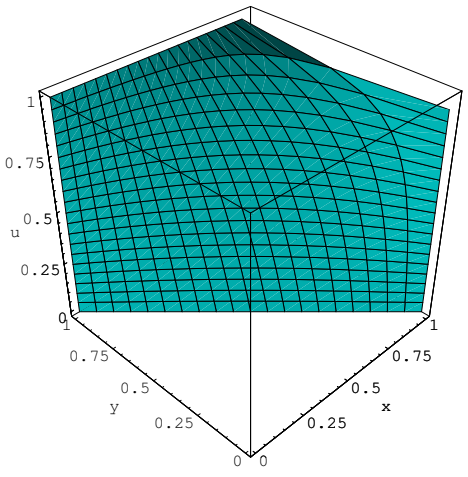

Figure 17 A direct plot of the solutions (e.g., $(x, (1-x)/(1-xy), y)$) shows "stretched" limits turning squares or triangles in (s,t) coordinates into pentagons in $[z_1, z_2, z_3, z_4, z_5]$-space.

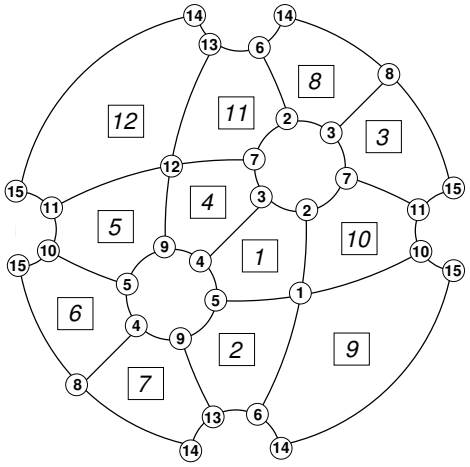

Figure 18 The 12 B_5 connected components without singularities.

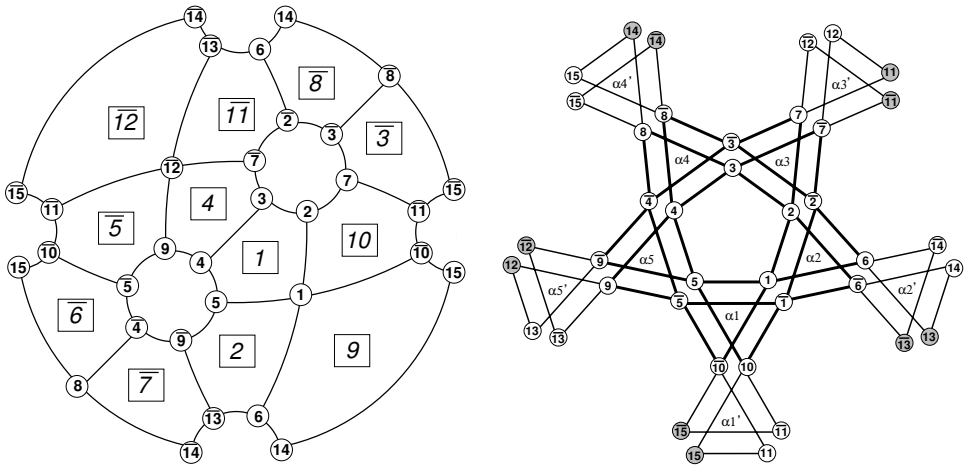

Figure 19 (a) The 12 B_5 connected components with double covering extensions noted by barred numbers. (b) Graph showing each vertex and the 10 hexagons corresponding to the double-covered $\mathbb{C}\mathbf{P}^1$ branch lines in the B_5 integrand.

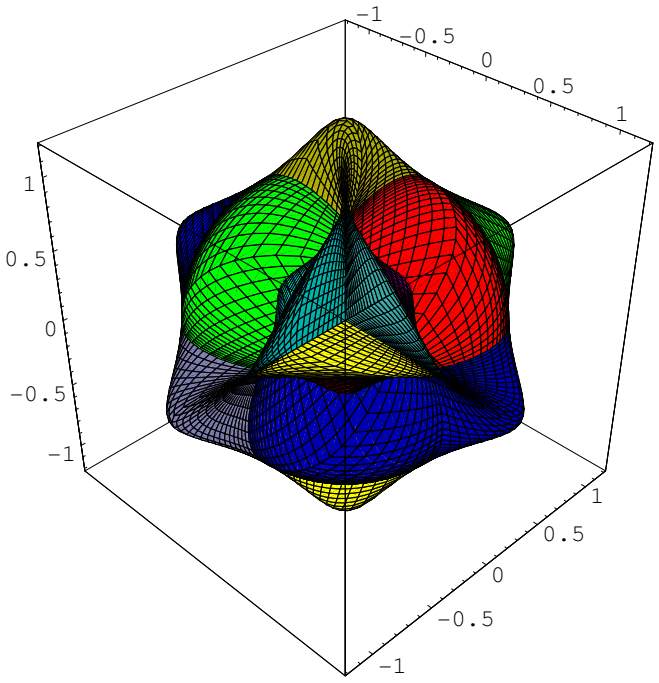

Figure 20 Genus 4 double cover of five-cross-cap surface projected from $\mathbb{R}^6$.

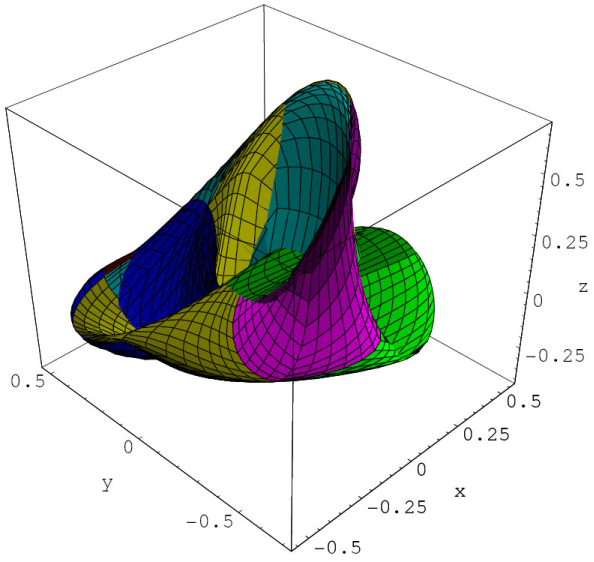

Figure 21 Projected embedding of the five-cross-cap surface itself.

corresponding to a sphere with *five cross-caps*. Figure 19 shows the solutions of the cross-ratio constraints, which double cover the five-cross-cap surface, and Figure 20 finally shows the visualization of the full double-covered surface embedded in $\mathbb{R}^6$. Creating an identified embedding of the five cross-cap surface itself (the single cover, not the double cover) employing the methods of ([4]) leads to the example image in Figure 21.

Much remains to be done to create further informative visualizations of these families of surfaces.

5 Discussion and Remarks

We have reviewed a family of basic problems in the complex analysis of one and many variables, and presented visualizations of a number of the manifolds that naturally arise. A new method, the use of cross-ratio variables instead of the expected $\mathbb{C}\mathbf{P}^N$ variables for the analysis of N complex variables, shows promise and is essential for the treatment of certain N-dimensional integrals. Among the surprising and unexpected aspects of this investigation was the discovery of a relationship to a family of objects known as the Stasheff associahedra ([7, 6, 2]). The explicit geometric embeddings that we discovered as part of our explicit graphics-oriented approach are in fact new *geometric* realizations of these *topological* objects.

Complex analysis is a fertile proving ground for developing and testing mathematical visualization methods. Here we have reviewed a variety of basic approaches that can be used for visualization in complex analysis, focusing on several families of complex algebraic equations and their geometry. Much remains to be done.

Acknowledgments

This research was supported in part by NSF grant numbers CCR-0204112 and IIS-0430730. Our thanks to Philip Chi-Wing Fu and Sidharth Thakur for assistance with graphics tools.

References

1 Élie Cartan. *The Theory of Spinors*. Dover, New York, 1981.

2 Satyan L. Devadoss. Tessellations of moduli spaces and the mosaic operad. In *Homotopy invariant algebraic structures. (Baltimore, MD, 1998)*, volume 239, pages 91–114, Providence, RI, 1999. Amer. Math. Soc.

3 A.J. Hanson. A construction for computer visualization of certain complex curves. *Notices of the Amer.Math.Soc.*, 41(9):1156–1163, November/December 1994.

4 Andrew J. Hanson and Ji-Ping Sha. A contour integral representation for the dual five-point function and a symmetry of the genus four surface in R^6. *Journal of Physics A: Mathematics and General*, 39:2509–2537, 2006. Web version at http://www.iop.org/EJ/abstract/0305-4470/39/10/017/ or on the arXiv at http://arxiv.org/abs/math-ph/0510064.

5 L.A. Pochhammer. Zur theorie der Euler'schen integrale. *Math. Ann.*, 35:495–526, 1890.

6 James Stasheff. Homotopy associativity of H-spaces. *Trans. Amer. Math. Soc.*, 108:275–292, 1963.

7 James Stasheff. *H-spaces from a Homotopy Point of View*. Lecture Notes in Mathematics 161. Springer Verlag, New York, 1970.

8 S.-T. Yau. On the Ricci curvature of a compact Kähler manifold and the complex Monge-Ampere equation. *Commun. Pure and Appl. Math.*, 31:339–411, 1978.